Green Chemistry

PAPER

View Article Online
View Journal | View Issue

Check for updates

Cite this: *Green Chem.*, 2018, **20**, 4920

High performance organic sodium-ion hybrid capacitors based on nano-structured disodium rhodizonate rivaling inorganic hybrid capacitors†

Ranjith Thangavel, [a] Rubha Ponraj,[b] Aravindaraj G. Kannan, [b] Karthikeyan Kaliyappan,[c] Dong Won Kim, [b] Zhongwei Chen [c] and Yun-Sung Lee *[a]

Received 26th June 2018,
Accepted 17th September 2018

DOI: 10.1039/c8gc01987h

rsc.li/greenchem

Sodium hybrid capacitors (NHCs) have tremendous potential to meet the simultaneous high energy–high power requirement of next-generation storage applications. But NHCs still face some obstacles due to poor sodium ion kinetics, low power, and poor cyclability while working with several inorganic sodium ion hosts. Additionally, developing high-performance NHCs that are sustainable and versatile is more crucial from the perspective of energy storage devices. Here, we report a conceptually new and high performance organic sodium hybrid capacitor (ONHC) system, developed by substituting a conventional toxic-metal-containing inorganic battery electrode of an NHC with a nano-structured, metal free, and renewable organic molecule – disodium rhodizonate – to host sodium ions. The sustainability of the ONHC is greatly enhanced by the simultaneous utilization of high surface area cardamom shell (as biomass)-derived porous carbon as a high-power capacitor electrode. The new system exhibits an outstanding performance, delivering a high energy density of ~87 W h kg^{-1} along with a high specific power of 10 kW kg^{-1} (based on the mass in both electrodes), outperforming inorganic sodium hosts. High durability over 10 000 cycles (~85% retention) with an ultra-low energy loss of ~0.15% per 100 cycles is also demonstrated, indicating its emergence as a rival to conventional metal containing lithium and sodium hybrid capacitors. The current study provides new opportunities for developing greener and sustainable devices beyond conventional systems for next-generation storage applications.

1. Introduction

Electrical energy storage (EES) devices delivering a simultaneous high energy–high power characteristic have generated tremendous attention for utilization in future electric vehicles and power-grid applications. Though batteries have a high energy density, their sluggish kinetics leads to inferior power behavior, impeding the output performance. The development of hybrid capacitor (HC) systems established a trade-off relationship between the merits of batteries and capacitors to deliver an enhanced energy output at a higher power and with a longer operation life. The simultaneous intercalation/deintercalation processes in a battery type electrode together with the adsorption/desorption process in a capacitor type electrode provides a high output energy under high-power conditions. Lithium hybrid capacitors (LHCs) have become commercially successful and are expected to be used in electric vehicles and hybrid electric vehicles in the future.

However, the limited lithium resources cannot fulfill the high industrial demand at a low price. This has diverted the research interest beyond lithium-based energy storage systems, and the quest for a competitive system is still under investigation. Sodium ion-based energy storage systems have evolved as capable alternatives to lithium-based systems owing to the wide availability of sodium and the similarity in the working chemistry of the two devices.[1,2] However, high power realization is more difficult in a battery configuration because of the large-sized sodium ion. Consequently, the research trend has shifted toward sodium-ion hybrid capacitors.[3,4] Sodium hybrid capacitors (NHCs) are a new class of devices with a strong potential to achieve high energy and high power with a longer stability due to the simultaneous occurrence of battery type intercalation/de-intercalation and capacitor type adsorption/

[a]Faculty of Applied Chemical Engineering, Chonnam National University, Gwangju 500-757, Korea. E-mail: leeys@chonnam.ac.kr
[b]Department of Chemical Engineering, Hanyang University, Seungdong-gu, Seoul 133-791, Korea
[c]Department of Chemical Engineering, University of Waterloo, Waterloo, Ontario N2L 3G1, Canada

†Electronic supplementary information (ESI) available. See DOI: 10.1039/c8gc01987h

desorption reactions. Thus, NHCs have the potential to be applied in next-generation devices.[5–7]

Research on battery type electrodes has considerably increased, including studies on $Na_3V_2(PO_4)_3$, hard carbon, MXenes, V_2O_5, Nb_2O_5, and $NaTi_3O_7$, to improve the performance of NHCs.[8–14] Very recently, high-performance NHC systems have been demonstrated to outperform their lithium analogues both in terms of energy and power densities, proving NHCs to be suitable alternatives to LHCs.[15–19]

The current urgent concern is to develop a green and versatile energy storage system without sacrificing the output performance.[20,21] However, highly toxic inorganic compounds are inevitable in EES devices, and the depleting inorganic resources could result in supply restrictions, increasing the global alarm regarding the sustainability, greenness, and cost of EES. Furthermore, overcoming the harmful and hazardous extraction processes for toxic inorganic complexes is essential to achieve a sustainable environment.[22,23] Intensive research has established metal-free, green, and eco-friendly organic compounds as next-generation clean energy storage materials, and they have been investigated for usage in organic lithium ion batteries and sodium ion batteries (SIBs).[24,25] To date, such green organic compounds have not been used in high energy–high power hybrid capacitor devices. The utilization of organic molecules in NHCs has resulted in the emergence of a new class of inorganic compound-free, green energy storage systems, namely, organic sodium hybrid capacitors (ONHCs), which could be promising for delivering high energy at a high power.

Various organic compounds with an active redox center to host Na^+ ions were studied for organic SIBs.[26–28] In the search for a potential candidate, disodium rhodizonate (DSRH) could be an appropriate choice to act as a green battery electrode in ONHCs, hosting sodium ions. Its numerous advantages, including a wide structural flexibility, tailored molecular design, easy tuning of the redox potential for multi-electron transfer reactions, light weight, high capacity, and abundant availability in nature, make this organic compound more benign for energy storage applications.[29–31] Additionally, DSRH, belonging to the keto–carbonyl group, having soft and flexible organic compounds, can be incorporated into large-sized sodium ions with a very low volume expansion and is favorable for delivering a high-current performance.[32]

However, the practical capacity, rate performance and cyclability of DSRH need a lot of improvement when used in fast working capacitor devices. It is well known that the sodium ion storage kinetics greatly depends on the morphology and size effects of the host material. In the present study, the sodium ion storage kinetics was improved by utilizing nano-structured DSRH synthesized by a facile antisolvent technique. In comparison with bulk commercial DSRH (bulk-DSRH) and high energy ball milled DSRH with reduced particle size (milled-DSRH), nano-structured DSRH (nano-DSRH) showed improved capacity, rate performance and stability.

To completely realize the eco-friendliness of a new ONHC, considerable attention must be paid to capacitor type adsorption electrodes. Capacitor type electrodes are generally composed of porous carbon, and their ion storage mechanism involves a simple double-layer formation at the electrode–electrolyte interface.[33] To date, commercially available activated carbon derived from coal and pitch has been used in a battery type electrode.[34] Utilization of materials from such exhaustible and environmentally hazardous resources could question the complete sustainability of an ONHC device.

As an alternative, biomass-derived porous carbon could be an excellent candidate for maintaining the eco-friendliness of ONHCs. Although biomass-derived porous carbon has been widely used in electrical double-layer capacitors and LHCs, there are not many reports on its application in NHCs, and it demands an extensive investigation. Biomass-derived porous carbon has the advantages of a high surface area, large pore volume, and ease of tailoring its morphology and surface functionalities, which could be beneficial for the fast accommodation of the large-sized solvated ions from the organic electrolyte.[35,36] The wide availability of waste biomass is highly advantageous for achieving a large-scale manufacturing process and facilitating the recycling of waste. A highly porous *in situ* nitrogen-doped cardamom shell-derived porous carbon (CDC) is known to have been utilized as a high-power capacitor electrode in ONHCs.

Herein, we report a conceptually new class of energy storage devices, namely, an ONHC fabricated by substituting a traditional toxic transition metal-containing Na^+ ion insertion compound with metal-free, green, and redox active commercial DSRH as an organic Na^+ ion host. Furthermore, to make the system still cleaner and greener, a highly porous biomass-derived carbon, *i.e.*, CDC, is utilized as a high-power adsorption electrode. The new ONHC device operates by establishing a trade-off relationship between the advantages of a battery and a capacitor, and it could emerge as a cleaner, greener, and a more sustainable alternative to conventional energy storage devices.

2. Experimental

Commercial DSRH was obtained and used directly without further processing for bulk-DSRH analysis. Commercial DSRH was milled for 1 h in a Pulverisette-6 planetary ball mill. For nano-DSRH, bulk-DSRH was dissolved in water (5 mg ml^{-1}) and mixed with ethanol in a ratio of 1 : 10 by volume. After 10 min sonication, DSRH precipitates were collected by vacuum filtration and then dried at 60 °C for 8 h under vacuum. Cardamom shells purchased from the local food market were used in this study. The seeds inside the cardamom shells were first removed, and the shells were thoroughly washed with water to remove any impurities and then dried at 120 °C for 48 h. The shells were then carbonized in air at 300 °C for 2 h and chemically activated with KOH at 750 °C for 1.5 h under an argon atmosphere. The weight ratio of the carbonized precursor to the pore-forming agent (KOH) was fixed at 1 : 5. The resultant products were washed with 0.1 M HCl,

and then washed several times with water and ethanol for neutralization. The products were next vacuum-dried at 120 °C for 24 h.

3. Characterization

3.1 Physical characterization

XRD patterns of all the samples were recorded using a Rigaku Rint 1000 (Japan) diffractometer using Cu Kα as the radiation source. The morphological features of the samples were determined using field emission SEM (FE-SEM) (S4700, Hitachi, Japan) and high-resolution TEM (HR-TEM) (Tecnai F20, Philips, Holland). Fourier transform infrared spectroscopy (FT-IR) was performed using a Nicolet FT-IR 200 from Thermo Scientific. Nuclear magnetic resonance (NMR) spectroscopy was conducted on a Bruker Avance 600 MHz spectrometer. The Raman spectra were recorded using a Raman dispersive spectrometer (LabRam HR 800 Horiba, Japan). Nitrogen adsorption and desorption isotherm measurements were performed using a Micromeritics ASAP 2010 analyzer. XPS was performed using a Multilab instrument (monochromatic Al Kα, radiation $h\gamma$ = 1486.6 eV).

3.2 Electrochemical characterization

DSRH electrodes were prepared using Ketjen black and PVDF as the conductive carbon and binder, respectively. The ratio of the active material to the conductive carbon and binder was maintained at 75 : 15 : 10. The produced slurry was pasted over a stainless-steel foil and dried at 120 °C for 12 h before use. The CDC and commercial activated carbon (CAC) cathode were prepared using Ketjen black and teflonized-acetylene black (TAB) as the conductive carbon and binder, respectively. The ratio of the active material to the conductive carbon and binder was maintained at 80 : 10 : 10. The slurry was then rolled over a stainless-steel mesh and dried at 160 °C for 4 h before use. The textural properties of CAC were given in our previous publication.[36] All the electrochemical measurements were performed in a standard CR2032 coin-cell assembled inside an argon-filled glove box. The half-cell performance of DSRH and CDC was tested against the Na metal, separated by a porous polypropylene (Celgard 3401, USA) separator. For the HC testing, the mass ratio of DSRH to CDC was kept at 1 : 1.5 and a mass loading of 1.8–2.4 mg cm^{-2} was maintained. The electrolyte used was $NaClO_4$ in ethylene carbonate (EC)/dimethyl carbonate (DMC) (1 : 1 vol/vol). CV and EIS studies were performed in a Bio-Logic (SP-150, France) electrochemical workstation. The galvanostatic charge/discharge studies were performed between 0 V and 3 V at different current densities using a Won-A-Tech WBCS 3000 (Korea) cycle tester. The energy density and power density were calculated using the formulae $E = (P \times t)$ W h kg^{-1} and $P = (IV/2)$ W kg^{-1}, respectively, where I is the current normalized to the active mass in both the electrodes (A g^{-1}), V is the working potential of the system (V), and t is the discharge time (s).

4. Results and discussion

The chemical structure of DSRH in Fig. 1a is a keto–carbonyl organic compound, composed of a six-membered carbon ring that includes a carbon–carbon double bond and four carbonyl groups.[37,38] The crystal structure of DSRH in Fig. 1b constitutes a layered structure with alternating hexagonally packed sodium ions (Na^+) and rhodizonate ($C_6O_6^{2-}$) layers, which is highly beneficial for easy and fast sodium insertion. The electron-rich keto–carbonyl groups are highly redox active sites for hosting Na^+ ions. Owing to its high lattice energy, DSRH can efficiently retain the Na–O ionic bond and exhibit excellent stability in organic electrolytes.[37] These favorable attributes of DSRH are highly analogous to the present inorganic sodium ion hosts, and DSRH could emerge as a suitable high-energy battery electrode for ONHCs. The X-ray diffraction (XRD) patterns of bulk-DSRH and nano-DSRH in Fig. 1c remain the same with a crystalline nature and exhibit an orthorhombic structure associated with the *Fddd* space group. However, milled-DSRH has a loss of crystallinity after the milling process where sharp peaks merge to form a broader one.

The scanning electron microscopy (SEM) images of various DSRH types are shown in Fig. 1d–f. Commercial bulk-DSRH shows the presence of microcrystals (~50 μm) with an octahedron-like morphology. The milled-DSRH shows a reduced particle size (~2 μm) even after 1 h of high energy ball milling. However, the nano-DSRH synthesized by the anti-solvent precipitation strategy shows the presence of agglomerated nano-sized particles (150–200 nm). The TEM images of the DSRH structures (Fig. 1g–i) further confirm the structural modification of bulk-DSRH after milling and the anti-solvent precipitation process. The selected area diffraction (SAED) pattern given in the inset of the TEM images shows the presence of diffuse rings with bright spots, indicating the polycrystalline nature of DSRH. The polycrystalline nature is retained even with milled-DSRH and nano-DSRH. The driving force for the formation of nano-DSRH is the rapid supersaturation of DSRH in an ethanol anti-solvent followed by crystallization in a water/ethanol mixture. The nano-morphology can lead to a fast capacitive reaction, resulting from the rapid ionic diffusion compared with the micron-sized DSRHs. Additionally, the highly conjugated organic structure with a high ionic and electronic conductivity can easily favor pseudocapacitive ion storage at high currents.[32] The chemical structure of all DSRH samples are verified by FT-IR and NMR spectroscopy and the results are given in Fig. S1.† The FT-IR spectra of milled-DSRH and nano-DSRH in Fig. S1a† exhibit a broad band between ~1400 and 1600 cm^{-1} corresponding to C=C and C=O. The spectra are similar to the FT-IR spectrum of bulk-DSRH (commercial sample), indicating that the functional groups are unchanged. In addition, ^{13}C-NMR of bulk-DSRH, milled-DSRH and nano-DSRH also reveals that the structures remain intact. Irrespective of the different morphological characteristics, bulk-DSRH, milled-DSRH, and nano-DSRH show similar chemical structures.

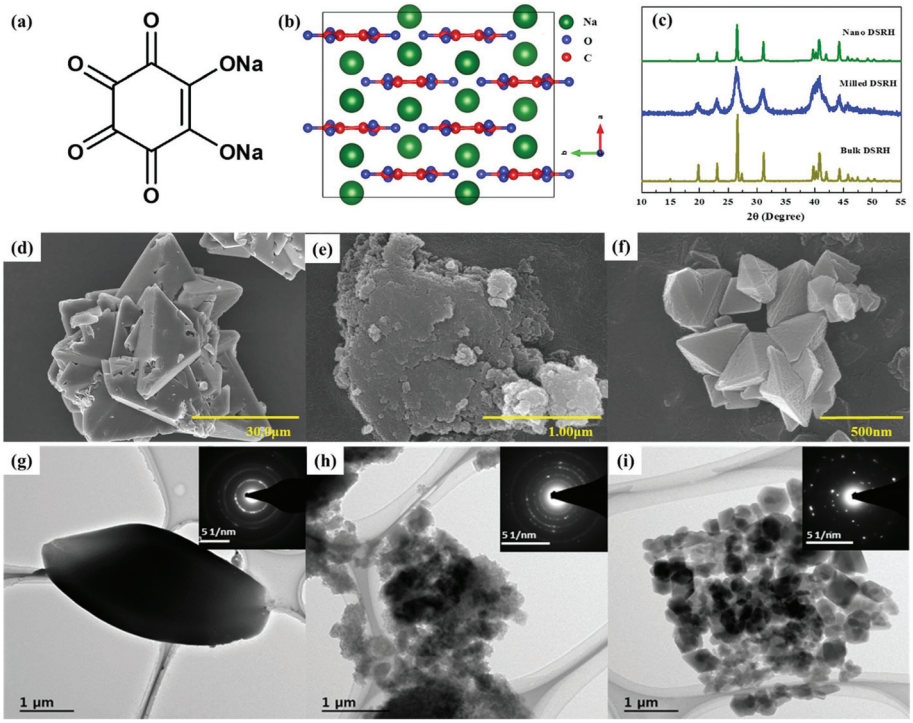

Fig. 1 (a) Chemical structure of DSRH, (b) the crystal structure of DSRH, (c) XRD patterns of DSRH, SEM images of (d) bulk-DSRH, (e) milled-DSRH, and (f) nano-DSRH, and TEM images and SAED patterns of (g) bulk-DSRH, (h) milled-DSRH, and (i) nano-DSRH.

The SEM images in Fig. S2a† show that the CDC particles are within a few micrometers, over which numerous pores are randomly distributed. Transmission electron microscopy (TEM) images of the CDC (Fig. S2b and c†) again confirm that the randomly distributed nanosized pores are less than 5 nm and are arranged in a hierarchical manner. The N_2-adsorption/desorption isotherm of the CDC (Fig. S3†) exhibits a combination of type I/IV isotherms with a high BET surface area of ~2200 m^2 g^{-1} and a large pore volume of 1.51 cm^3 g^{-1}.[39] It reveals a narrow pore distribution of small mesopores and micropores, among which ~26% are mesopores and 74% are micropores. The XRD patterns of the CDC shown in Fig. S4a† depict a highly amorphous nature with broad graphitic peaks at approximately 23° and 44°, indicating a highly disordered and turbostratic nature of the CDC. The *d*-spacing (002 plane) of the CDC is calculated to be 0.378 nm, which is larger than that of graphite (0.355 nm), emphasizing the broadening of the graphitic planes after KOH activation.[33] The Raman spectrum of the CDC (Fig. S4b†) exhibits two characteristic bands: (i) a G band at ~1594 cm^{-1} related to the in-plane vibrational graphitic domains and (ii) a D band at ~1349 cm^{-1} related to the defect and disorder bands in the CDC. The I_D/I_G ratio is calculated to be ~1.03.

The surface nature of the CDC was examined by X-ray photoelectron spectroscopy (XPS), and the results are displayed in Fig. S5a.† The complete XPS survey spectrum of the CDC shows the presence of carbon and oxygen along with nitrogen. The numerous nitrogen containing minerals and acids in the cardamom shells could be the source of the nitrogen heteroatoms that get incorporated into the carbon framework during carbonization and activation. The other metal impurities in the CDC are under the detection limit of XPS as it is removed during the acid washing step. The deconvoluted C 1s and N 1s spectra of the CDC are illustrated in Fig. S5b and c,† respectively. The C 1s spectrum displays a dominating central peak at ~284.6 eV, corresponding to C–C bond sp^2-hybridized carbon. The short peaks at ~286 eV (C=O) and ~288.5 eV (O–C=O) indicate the presence of oxygen containing functional groups.[40] The deconvoluted N 1s spectrum shows peaks at ~398.3 eV, ~399.8 eV, and ~401.1 eV, indicating the contribution from pyridine, pyrrole, and a quaternary type nitrogen. These contribute toward the enhancement of the electronic conductivity of the carbon framework.[41]

The hybrid porous architecture along with the nitrogen heteroatoms in the CDC could render enhanced kinetics for double-layer adsorption. The mesopore channels ensure a short ion-flow path to deeper micropores under high-current conditions, thereby involving the micropores in an active ion adsorption process. By providing a high surface area along with large mesopores, biomass CDC could be a promising high-power capacitor electrode for ONHCs.[42]

4.1 Half-cell performance

The charge–discharge (CD) curves of all DSRH at 0.1 A g^{-1} are shown in Fig. S6.† The series of consecutive symmetrical plateaus in the CD profile indicate a sequential sodium ion

capture by the keto–carbonyl groups *via* a highly reversible redox reaction.[32] The plateaus in milled-DSRH are less pronounced when compared with nano- and bulk-DSRH, yet showed a higher capacity than bulk-DSRH. However, nano-DSRH showed a high capacity and clear plateau along with low polarization. This is attributed to the nano size effect of DSRH which greatly improved the sodium ion storage kinetics. The CD curves of nano-DSRH at different current densities are shown in Fig. 2a. A high discharge capacity of ~188 mA h g^{-1} is obtained at a 0.1 A g^{-1} current density. A remarkable rate performance is exhibited by nano-DSRH, delivering ~112 mA h g^{-1} at 5 A g^{-1} along with a superior recovery capacity of ~183 mA h g^{-1} at 0.1 A g^{-1} (Fig. 2b). Even at 50 orders of enhanced current, the specific capacity utilization is very high, and the excellent rate performance can be ascribed to the fast charge transfer kinetics in the layered structure and the rapid redox reaction between the sodium ions and carbonyl groups.[37,43] In contrast, bulk-DSRH and milled-DSRH showed poor capacity retention and capacity recovery. Bulk-DSRH delivered a capacity of ~111.1 mA h g^{-1} and 24 mA h g^{-1} at 0.1 A g^{-1} and 5 A g^{-1}, respectively, and milled-DSRH delivered ~185 mA h g^{-1} and 74 mA h g^{-1} at 0.1 A g^{-1} and 5 A g^{-1}, respectively. Substituting the kinetically slow intercalation compounds with nano-structured DSRH organic hosts could increase the possibility of high-power sustainable EES. The ion transfer kinetics of various structured DSRH types is evaluated by the electrochemical impedance spectroscopy technique and given in Fig. S7.† The Nyquist plots of DSRH show a semicircle at the high frequency region and a Warburg tail at the low frequency region ascribed to interface resistance and ion diffusion resistance, respectively. The interface resistance that involves contact and charge transfer resistances is lower for nano-DSRH than that for milled-DSRH and bulk-DSRH. The reduction in interface resistance indicates that nano-DSRH can exhibit an improved and rapid kinetics than bulk-DSRH and milled-DSRH. Most importantly, an outstanding capacity retention of ~85% and a coulombic efficiency of ~100% are demonstrated by nano-DSRH even after 500 cycles at 2.5 A g^{-1} (Fig. 2c). In contrast, bulk-DSRH and milled-DSRH retained ~74% and 69% of the initial capacity, respectively. The CD curves of nano-DSRH remain the same throughout the cycling (Fig. 2d), emphasising a reversible sodium ion storage mecha-

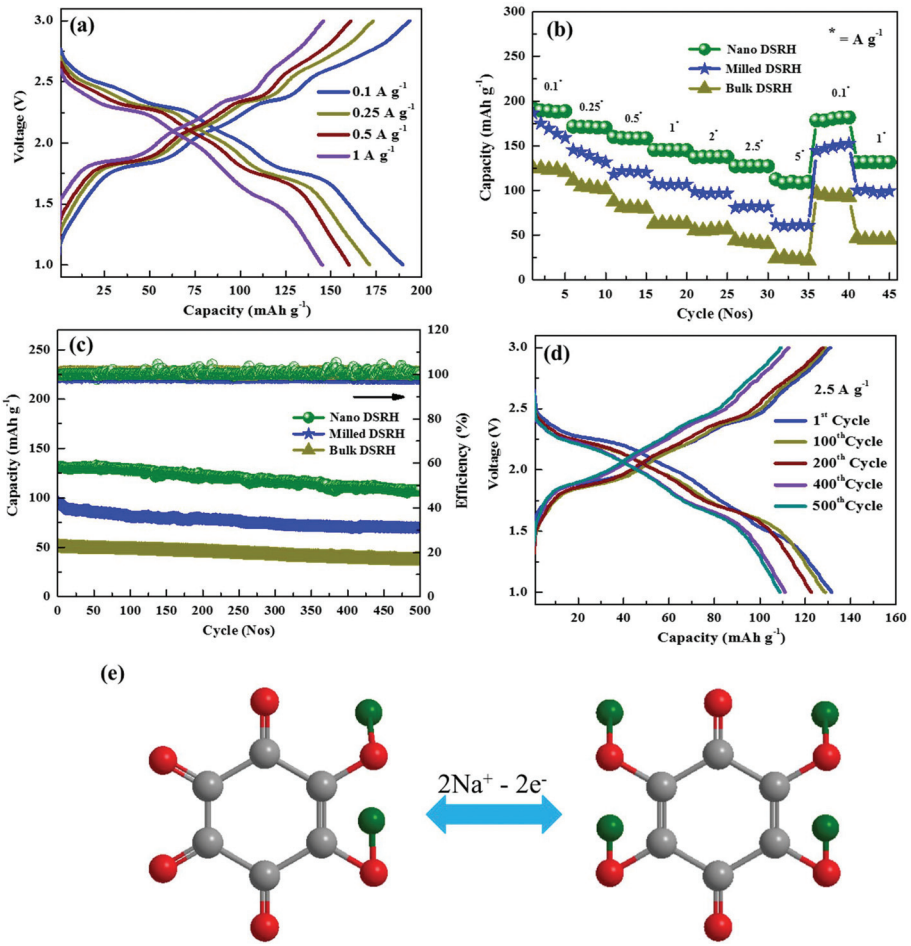

Fig. 2 (a) CD curves of nano-DSRH *vs.* Na, (b) rate performance of DSRH *vs.* Na in the range of 3–1 V, (c) cycling stability of DSRH, (d) CD curves of nano-DSRH at different cycles (2.5 A g^{-1}), and (e) the scheme of the sodium ion storage mechanism in DSRH.

nism. The sodium ion storage mechanism in DSRH is shown in Fig. 2e.

To elucidate the fast sodium ion storage behavior of nano-DSRH, cyclic voltammetry (CV) was performed at different scan rates. The corresponding CV curves in Fig. 3a display a series of four consecutive redox peaks in both the cathodic and anodic scans. During the cathodic scan, the peaks are centered at ~2.46 V, 2.27 V, 2.04 V, and 1.72 V, whereas during the subsequent anodic scan, the peaks are centered at ~1.87 V, 2.11 V, 2.36 V, and 2.62 V. This indicates a highly reversible and sequential sodium insertion in nano-DSRH *via* a four-electron redox process.[32,44] Even with the increase in the scan rate, nano-DSRH preserves the shape of the CV curves, and the redox peaks are clearly visible. The highly symmetrical and identical redox peaks even at higher scan rates suggest a facile sodium insertion even under high-power conditions.

The current (i) *vs.* scan rate (ν) relationship from the equation $i = a\nu^b$ (a and b are adjustable parameters) depicts the nature of sodium storage in DSRH. A b-value closer to "0.5" implies diffusion-controlled intercalation storage, whereas a b-value closer to "1" implies that the dominant capacity contribution is from surface-limited pseudocapacitive surface storage.[45] Fig. 3b shows the plot of log(i) *versus* log(ν) derived from the maximum output current in the anodic and cathodic scans at different scan rates. The "b-value" obtained from the slope of the linear fit is approximately 1, indicating that the major current contribution is from surface-induced pseudocapacitive sodium storage.[46] Such a fast pseudocapacitive sodium is favorable for achieving a high energy even under high-current conditions in the ONHC. In contrast, sluggish diffusion-limited sodium storage in a battery type electrode of an ONHC will cause a high energy loss at high power. However, with fast surface-limited ion storage, the energy loss at high power could be easily curtailed.

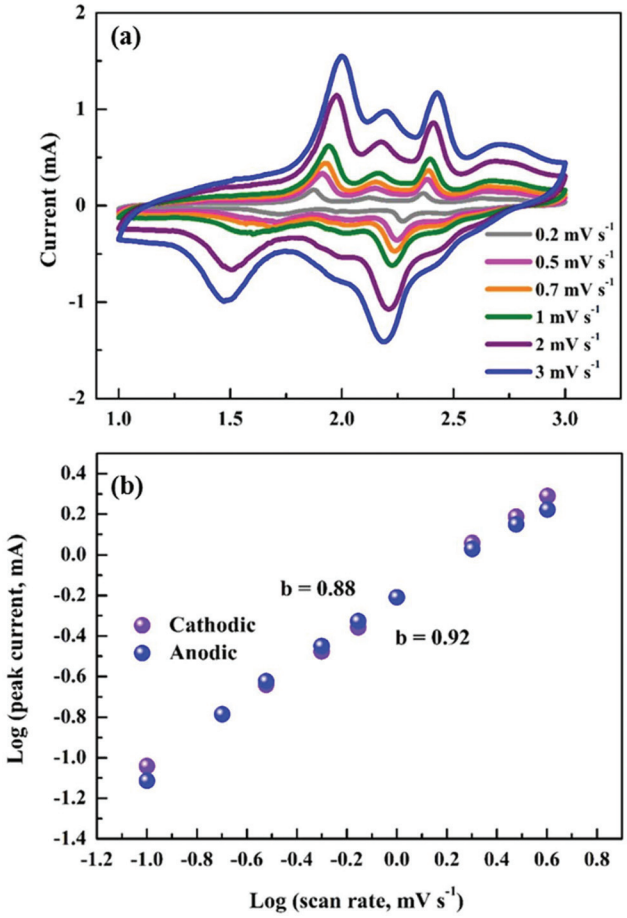

Fig. 3 (a) Cyclic voltammetry (CV) curves of nano-DSRH *vs.* Na and (b) current *vs.* scan rate relationship obtained from the CV curves.

To understand the phase change in nano-DSRH, the crystal structure of DSRH is evaluated after cycling using the XRD technique (Fig. S8†). Cycled nano-DSRH loses almost all of its crystallinity and an evolution of completely new peaks which did not match with its original phase is noted. This is attributed to the formation of the most stable and new γ-phase from the α-phase following the first sodiation process. The newly formed γ-phase of DSRH also has a layered structure where C_6O_6 layers lie directly over each other and this new phase takes a different path for sodium ion storage.[47] This is confirmed by the change in the discharge curve patterns of DSRH after the first sodiation process (Fig. S9a†). However, the CD curve pattern appears well maintained throughout from the second sodiation process. Additionally, this phase change and the new sodiation path from the second cycle are also verified by CV studies (Fig. S9b†), where the 1st cathodic scan and the 2nd cathodic scan show different storage patterns, but the patterns are well maintained after the second scan, and this phenomenon is correlated with the CD curves obtained. However, this phase change does not affect the sodium ion storage process as high capacity and high rate performance are attained along with high stability.[20] FE-SEM images are recorded for nano-DSRH after 1st discharge (Fig. 4a) and consecutive charge (Fig. 4b), and the morphology of DSRH does not show any significant changes. Even after 100 cycles, the morphology of nano-DSRH is well maintained (Fig. 4c), indicating its structurally stable nature.

The sodium ion kinetics in nano-DSRH is further investigated using the electrochemical impedance spectra (EIS) and the results are presented in Fig. 4d and e. The Nyquist plots of fresh nano-DSRH cells show a large semi-circle at high frequency attributed to charge transfer resistance, followed by a Warburg impedance tail at low frequency, indicating the diffusion of sodium ions into the electrode. After the first discharge process (sodiation to 1 V *vs.* Na), the Nyquist plot displays two semi-circles confirming the sodiation of nano-DSRH. On subsequent charge (desodiation to 3 V *vs.* Na), the semicircle in the mid-frequency range disappeared and instead a single semicircle with a lower charge transfer than the fresh cell, indicating better electron and sodium ion kinetics, as shown in Fig. 4d, appeared. In addition, even after cycling, the increase in charge transfer resistance (Fig. 4e) is very negligible indicating a fast and stable charge–discharge process.

The outstanding high current and the cycling behavior of organic compounds are highly attractive when compared with

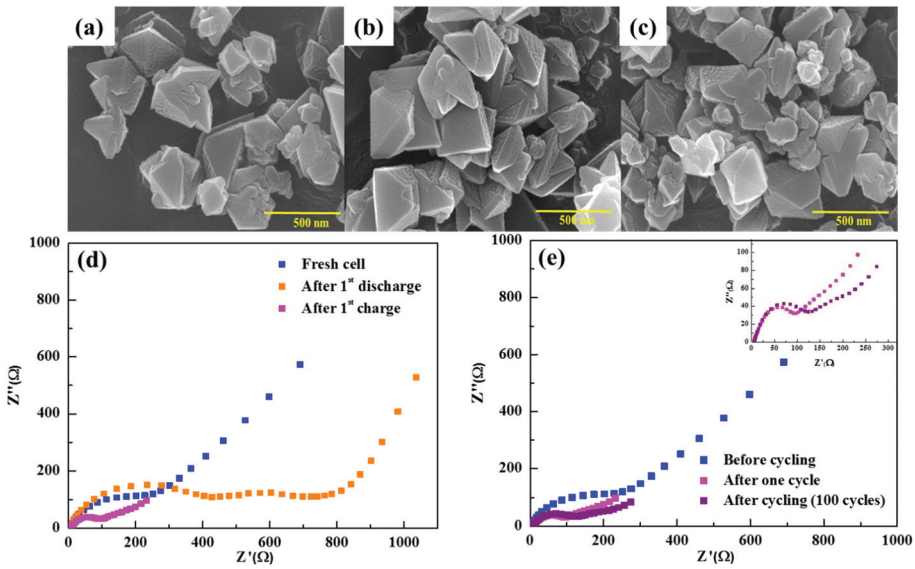

Fig. 4 SEM images of nano-DSRH (a) after 1st discharge, (b) after 1st charge, and (c) after 100 cycles, and (d) and (e) Nyquist plots of nano-DSRH at different states.

those of the inorganic insertion compounds. The fast and reversible sodium intake and release *via* a pseudocapacitive reaction minimizes the energy loss and enables a robust stability, ensuring the development of a new class of high energy storage devices.

The CD curves of the CDC are presented in Fig. 5a to examine their adsorption behavior. A linear and non-deviating CD curve between 3 and 4.5 V *vs.* Na corresponds to a pure surface adsorption reaction over the CDC pores.[48] The CDC delivers an impressive discharge capacity of ~70 mA h g^{-1}, equivalent to ~152 F g^{-1} at 0.25 A g^{-1}. Significantly, on increasing the current density to 8 A g^{-1}, the CDC maintains a remarkable capacity of ~24 mA h g^{-1} (55 F g^{-1}) (inset, Fig. 5a). Notably, the CDC demonstrates excellent stability, retaining ~90% of the initial capacitance even after 3000 cycles (Fig. 5b). Compared with previously studied adsorption electrodes for HCs, the CDC exhibits better rate performance and stability, suggesting the use of bio-derived porous carbon as a high-power and long-life adsorption electrode for ONHCs.[6] The observed superior properties of the CDC are attributed to its highly porous nature along with the micro–mesopore architecture, which is highly favorable for ion accumulation. The ions continuously flow through the mesopore channels to deeper sub-micropores, are stored in the ionic reservoirs, and actively participate in the adsorption reaction. The large pore volume of the CDC could store a large volume of the electrolyte for a longer time and thereby ensure the longevity of the adsorption reaction.[21,49–51]

4.2 Organic sodium hybrid capacitor

Considering the remarkable performance of nano-DSRH compared with bulk- and milled-DSRH, nano-DSRH is further studied for use in hybrid capacitor applications in the 0–3 V

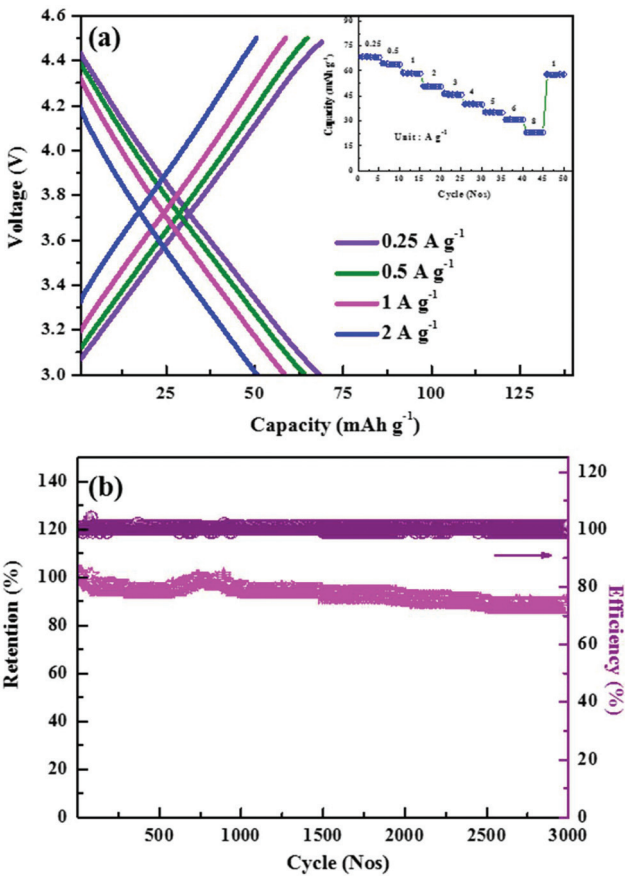

Fig. 5 (a) Charge/discharge curves of CDC, Inset: rate performance, and (b) the cycling stability of CDC.

range. The CV curves of the fabricated ONHC are presented in Fig. 6a. Unlike the electrical double-layer capacitors (EDLCs) that show a rectangular CV shape profile, the ONHC exhibits a shape profile with two different regions: (i) a broad rectangular capacitive region owing to the anionic adsorption/desorption occurring in the CDC and (ii) a reversible redox region owing to the simultaneous Na ion insertion in/extraction from the carbonyl groups of DSRH.[52,53] The shape profile is well maintained with the increasing scan rate, and the redox peaks are clearly visible even at a high scan rate, implying that the sodium insertion occurs even at high scan rates. Furthermore, the linear relationship between the output current and the scan rate indicates a fast surface-limited capacitive reaction (Fig. 6b). Substituting the sluggish diffusion-limited reaction with a surface-limited reaction strongly supports the realization of high-power ONHCs.[3,54] The dual energy storage behavior simultaneously integrates the functions of both a battery and a capacitor, providing a significant advantage for achieving a high-energy output at a high power rate. The scheme of the working mechanism of the ONHC is shown in Fig. 6c.

The CD curves of the ONHC at different current densities are displayed in Fig. 7a and S10.† The voltage–time shape profile of the ONHC is not linear, deviating from the typical triangular curves exhibited by EDLCs, confirming its dual energy storage behavior.[9,20,52,55] A series of humps/deviations are observed in the shape profile, implying a sequential sodium insertion in DSRH, which is in agreement with the CV profile behavior. The CD curves maintain the shape profile with continuous cycling, without any deterioration, confirming a highly reversible and energy storage reaction mechanism of the ONHC. The ion storage mechanism of the ONHC is as follows: (i) on charging, the sodium ions from the electrolyte are inserted into the keto–carbonyl groups of DSRH *via* a redox reaction along with a simultaneous anionic adsorption in the pores of the CDC and (ii) during discharge, the inserted sodium ions are extracted along with the simultaneous anionic desorption from the CDC. The above dual-ion storage reaction mechanism is highly reversible even under high-current conditions and can achieve high energy retention under high-power conditions. The continuous CD curves in Fig. 7b show a similar shape profile, indicating that the storage reaction mechanism is highly reversible. From the discharge time, the energy density and power density of the ONHC are calculated and presented in the Ragone plot in Fig. 7c and d. A maximum energy density of ~87 W h kg^{-1} and a maximum power of ~10 kW kg^{-1} (based on the active mass in both the electrodes) are achieved, and even at such a high power density, the ONHC retains a gravimetric energy of ~12 W h kg^{-1}. The energy–power behavior of the ONHCs employing the CAC cathode is also evaluated and the corresponding Ragone plot is shown in Fig. S11.† The energy obtained utilizing the CAC cathode is far lower than that using NHCs employing the CDC cathode. NHCs employing the CAC cathode fail at high currents because of considerable ion-diffu-

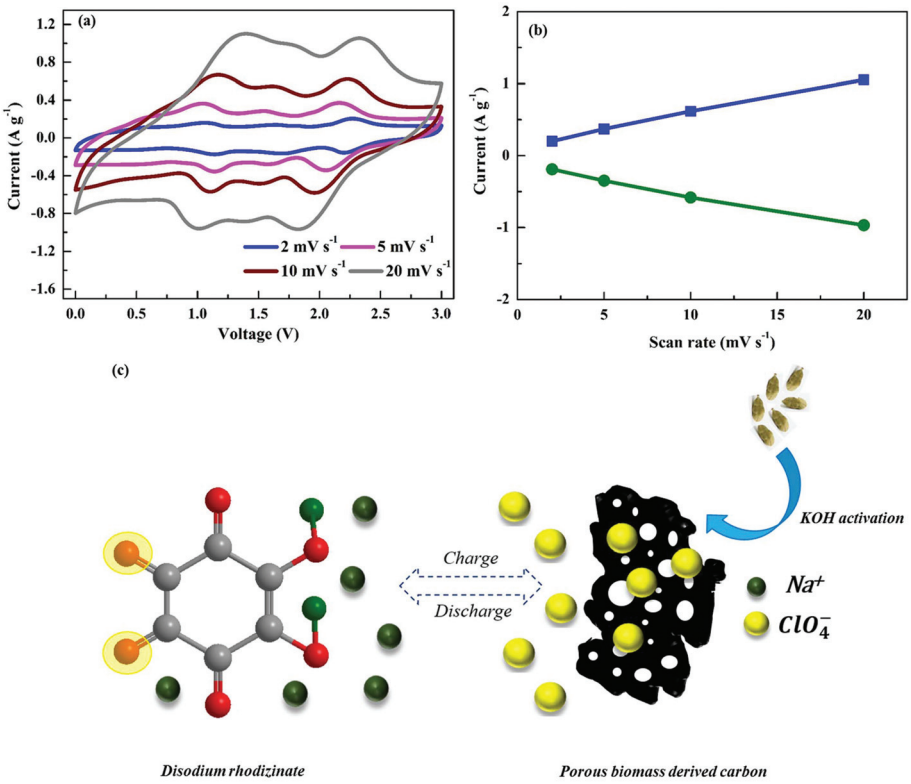

Fig. 6 (a) CV curves of the ONHC at 0–3 V at different scan rates, (b) output current *vs.* scan rate relationship obtained from the CV curves of the ONHC, and (c) the scheme of the working mechanism of the ONHC.

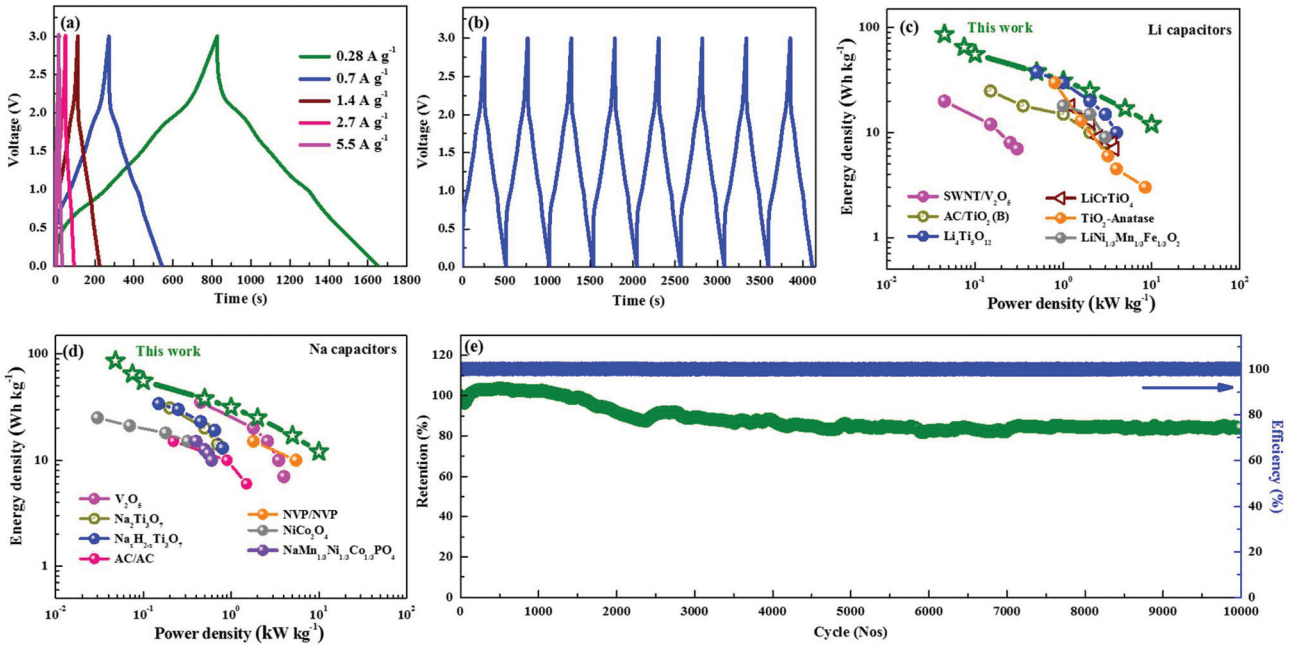

Fig. 7 (a) CD curves of the ONHC at different current densities, (b) continuous CD curves of the ONHC at 0.7 A g^{-1}, (c) and (d) Ragone plot comparing the performance of the ONHC with those of other capacitor systems, and (e) the cycling stability of the ONHC at 4 A g^{-1}.

sional losses in microporous activated carbon. However, NHCs employing CDC as the cathode performed well with high energy retention due to the favorable textural and surface properties of the green carbon. The ONHC energy density obtained is much higher than the energy output of EDLCs, and its output specific power surpasses the power of batteries, covering a wide range, bridging the gap between the low-power batteries and low-energy supercapacitors. The electrochemical performance of the ONHC is highly competitive and it outperforms the conventional LHCs and NHCs utilizing inorganic insertion hosts.[56,57] The Ragone plots in Fig. 7c and d compare the output performance of the ONHC with other HCs, and it clearly shows its higher performance than the widely investigated lithium and sodium HCs utilizing various ion hosts such as $Li_4Ti_5O_{12}$, TiO_2, V_2O_5, Nb_2O_5, $NiCo_2O_4$ and $Na_3V_2(PO_4)_3$ and many more.[58–63]

Stability is the most significant parameter for HCs, and the long-term performance of the ONHC was tested at specific current density of 4 A g^{-1}. The new ONHC exhibits high performance for 10 000 cycles with an energy loss of 0.15% per 100 cycles with ~100% coulombic efficiency (Fig. 7e). A slight increase in the capacitance is noted initially, which could be attributed to the delayed electrolyte infiltration in the organic and porous carbon electrodes. This activates the innermost electrode particles for electrochemical storage, and such a phenomenon has been observed previously for both organic type and carbon electrodes. An ultra-low energy loss of only 4% is noted from the 2000th cycle. Table S1† compares the output performance of the ONHC with conventional HCs, and it provides evidence of the superiority of the new ONHC, showcasing that it could be a powerful and analogous alternative. The Ragone plot in Fig. 8a confirms the high energy–high power behavior of the ONHC that eminently bridges the performance gap between high energy batteries and high power capacitors, thereby emerging as a prominent alternative. To further elucidate the high stability performance, EIS studies were conducted for the ONHC. It can be clearly seen in the Nyquist plot (Fig. 8b) that it contains a depressed semi-circle at high frequency indicating the charge transfer reaction and a Warburg tail at low frequency ascribed to sodium ion diffusion into the electrode. Even after long cycling, the charge transfer change in the ONHC is negligible, indicating the facile ion transfer kinetics between the electrodes.[64–67] The XRD patterns of the DSRH electrodes after cycling in Fig. S12† show a nearly amorphous nature and it could be attributed to the phase change from the new α-phase to the γ-phase during the initial cycles as discussed earlier. The SEM images show that the morphology of DSRH is well retained after 10 000 cycles, indicating a robust structural stability (Fig. S13†). The stability result reveals that the extraordinary stability of the ONHC surpasses that of the previously reported conventional HCs utilizing metal oxides, where the continuous structural deterioration impedes the long-term performance of the HC device. This achieved power and high stability are strongly analogous to the NHCs constructed with the intercalation type battery electrode.[68–70] The excellent stability and high coulombic efficiency of the ONHC can be attributed to the highly reversible nature of the storage reactions without a large structural change. From the results, it can be clearly seen that substituting the inorganic compounds with organic hosts could help develop green and eco-friendly high-performing ONHCs. Moreover, the conceptually novel ONHC could be a significant

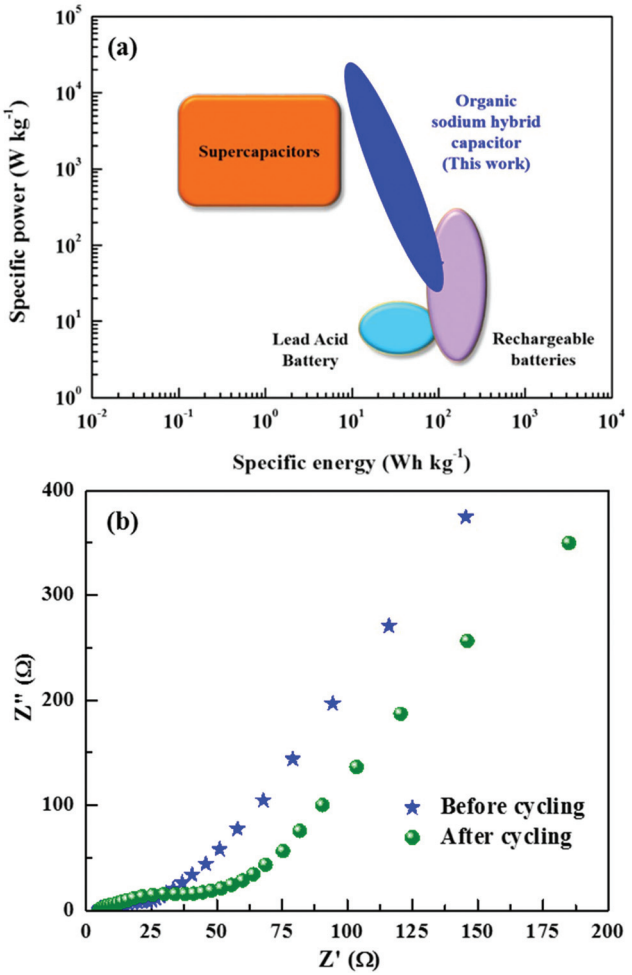

Fig. 8 (a) Ragone plot comparing the ONHC with other energy storage systems and (b) Nyquist plots of the ONHC.

alternative for the current energy storage systems and emerge as the next-generation green high energy–high power storage device.

The high performance of the ONHC can be mainly attributed to (i) the favorable two-dimensional layered DSRH structure, allowing easy insertion of numerous sodium ions, delivering a high capacity, (ii) fast and highly reversible pseudocapacitive sodium ion storage in nano-structured DSRH, synergistically elevating the energy density at high power, (iii) the structural flexibility owing to the less rigid and conjugated nature of the quinone compounds compared with the inorganic analogues, facilitating easy kinetics, the accommodation of large-sized sodium ions, and the achievement of high stability, (iv) biomass-derived carbon with a large surface area and hierarchical porosity, providing a wide electrode–electrolyte interface for high ion storage, (v) the presence of nitrogen heteroatoms in the carbon framework enhancing the electronic conductivity of the capacitor electrode and reducing the ion transport resistance, (vi) mesopore channels engaging even the deeper micropores for fast adsorption reactions by providing a shorter electron travel path, (vii) Na–O ionic bonds in DSRH retention owing to the high lattice energy, thereby maintaining good stability under robust cycling conditions in an organic electrolyte, and (viii) a high pore volume and a strong carbon framework withholding a large quantity of the electrolyte, providing high flexibility against the mechanical stress under high-current conditions.

5. Conclusion

We developed for the first time a new organic sodium hybrid capacitor system by substituting the traditional toxic-metal-containing inorganic sodium host with a redox-active and nano-structured organic sodium ion host. The organic sodium hybrid capacitor exhibited a high gravimetric energy density of up to ~87 W h kg^{-1} and a high power density of ~10 kW kg^{-1} (based on the active mass of both the electrodes) along with a robust stability over 10 000 cycles, outperforming the conventional hybrid capacitor systems. The current work demonstrated that the organic hybrid capacitors could be effective devices for bridging the performance gap between batteries and capacitors. The simultaneous utilization of organic molecules to host cations and biomass-derived carbon to store anions could result in the development of toxic metal-free, clean, and green next-generation sustainable energy storage devices. Furthermore, an in-depth study of various organic redox molecules could provide numerous opportunities to design and develop a high-performance high-energy–high-power organic device for future applications, similar to the current conventional systems.

Conflicts of interest

The authors declare no conflicts of interest.

Acknowledgements

This work was supported by the National Research Foundation of Korea (NRF) grant funded by the Korea government (Ministry of Science, ICT & Future Planning) (No. 2016R1A4A1012224).

References

1 H. Kim, H. Kim, Z. Ding, M. H. Lee, K. Lim, G. Yoon and K. Kang, *Adv. Energy Mater.*, 2016, **6**, 1600943.
2 S. Gao, Y. Sun, F. Lei, L. Liang, J. Liu, W. Bi, B. Pan and Y. Xie, *Angew. Chem., Int. Ed.*, 2014, **53**, 12789–12793.
3 Z. Chen, V. Augustyn, X. Jia, Q. Xiao, B. Dunn and Y. Lu, *ACS Nano*, 2012, **6**, 4319–4327.
4 R. Thangavel, B. Moorthy, D. K. Kim and Y.-S. Lee, *Adv. Energy Mater.*, 2017, **7**, 1602654.

5 R. Thangavel, A. G. Kannan, R. Ponraj, M.-S. Park, H. Choi, D.-W. Kim and Y.-S. Lee, *Adv. Mater. Interfaces*, 2018, 1800472.
6 J. Ding, H. Wang, Z. Li, K. Cui, D. Karpuzov, X. Tan, A. Kohandehghan and D. Mitlin, *Energy Environ. Sci.*, 2015, **8**, 941–955.
7 B. Li, J. Zheng, H. Zhang, L. Jin, D. Yang, H. Lv, C. Shen, A. Shellikeri, Y. Zheng, R. Gong, J. P. Zheng and C. Zhang, *Adv. Mater.*, 2018, 1705670.
8 S. Dong, L. Shen, H. Li, G. Pang, H. Dou and X. Zhang, *Adv. Funct. Mater.*, 2016, **26**, 3703–3710.
9 F. Wang, X. Wang, Z. Chang, X. Wu, X. Liu, L. Fu, Y. Zhu, Y. Wu and W. Huang, *Adv. Mater.*, 2015, **27**, 6962–6968.
10 X. Wang, S. Kajiyama, H. Iinuma, E. Hosono, S. Oro, I. Moriguchi, M. Okubo and A. Yamada, *Nat. Commun.*, 2015, **6**, 6544.
11 H. Wang, C. Zhu, D. Chao, Q. Yan and H. J. Fan, *Adv. Mater.*, 2017, **29**, 1702093.
12 C. Wang, F. Wang, Z. Liu, Y. Zhao, Y. Liu, Q. Yue, H. Zhu, Y. Deng, Y. Wu and D. Zhao, *Nano Energy*, 2017, **41**, 674–680.
13 J. Niu, J. Liang, R. Shao, M. Liu, M. Dou, Z. Li, Y. Huang and F. Wang, *Nano Energy*, 2017, **41**, 285–292.
14 J. Cui, S. Yao, Z. Lu, J.-Q. Huang, W. G. Chong, F. Ciucci and J.-K. Kim, *Adv. Energy Mater.*, 2017, 1702488.
15 H. Wang, D. Mitlin, J. Ding, Z. Li and K. Cui, *J. Mater. Chem. A*, 2016, **4**, 5149–5158.
16 D. Xu, D. Chao, H. Wang, Y. Gong, R. Wang, B. He, X. Hu and H. J. Fan, *Adv. Energy Mater.*, 2018, 1702769.
17 R. Wang, S. Wang, Y. Zhang, D. Jin, X. Tao and L. Zhang, *J. Mater. Chem. A*, 2018, **6**, 1017–1027.
18 Y.-E. Zhu, L. Yang, J. Sheng, Y. Chen, H. Gu, J. Wei and Z. Zhou, *Adv. Energy Mater.*, 2017, **7**, 1701222.
19 B. Yang, J. Chen, S. Lei, R. Guo, H. Li, S. Shi and X. Yan, *Adv. Energy Mater.*, 2017, 1702409.
20 R. Thangavel, K. Kaliyappan, D.-U. Kim, X. Sun and Y.-S. Lee, *Chem. Mater.*, 2017, **29**, 7122–7130.
21 H. Wang, J. Deng, C. Xu, Y. Chen, F. Xu, J. Wang and Y. Wang, *Energy Storage Mater.*, 2017, **7**, 216–221.
22 W. Deng, Y. Shen, J. Qian, Y. Cao and H. Yang, *ACS Appl. Mater. Interfaces*, 2015, **7**, 21095–21099.
23 Z. Song and H. Zhou, *Energy Environ. Sci.*, 2013, **6**, 2280–2301.
24 B. Häupler, A. Wild and U. S. Schubert, *Adv. Energy Mater.*, 2015, **5**, 1402034.
25 K. Chihara, N. Chujo, A. Kitajou and S. Okada, *Electrochim. Acta*, 2013, **110**, 240–246.
26 H. Banda, D. Damien, K. Nagarajan, M. Hariharan and M. M. Shaijumon, *J. Mater. Chem. A*, 2015, **3**, 10453–10458.
27 M. Miroshnikov, K. P. Divya, G. Babu, A. Meiyazhagan, L. M. Reddy Arava, P. M. Ajayan and G. John, *J. Mater. Chem. A*, 2016, **4**, 12370–12386.
28 F. Xu, H. Wang, J. Lin, X. Luo, S.-a. Cao and H. Yang, *J. Mater. Chem. A*, 2016, **4**, 11491–11497.
29 K. Chihara, N. Chujo, A. Kitajou and S. Okada, *Electrochim. Acta*, 2013, **110**, 240–246.
30 W. Ai, W. Zhou, Z. Du, C. Sun, J. Yang, Y. Chen, Z. Sun, S. Feng, J. Zhao, X. Dong, W. Huang and T. Yu, *Adv. Funct. Mater.*, 2017, **27**, 1603603.
31 Q. Zhao, Y. Lu and J. Chen, *Adv. Energy Mater.*, 2017, **7**, 1601792.
32 Y. Wang, Y. Ding, L. Pan, Y. Shi, Z. Yue, Y. Shi and G. Yu, *Nano Lett.*, 2016, **16**, 3329–3334.
33 X. Zhou, F. Chen, T. Bai, B. Long, Q. Liao, Y. Rena and J. Yang, *Green Chem.*, 2016, **18**, 2078–2088.
34 H. Wu, Y. Zhang, L. Cheng, L. Zheng, Y. Li, W. Yuan and X. Yuan, *Energy Storage Mater.*, 2016, **5**, 8–32.
35 G. Xu, J. Han, B. Ding, P. Nie, J. Pan, H. Dou, H. Li and X. Zhang, *Green Chem.*, 2015, **17**, 1668–1674.
36 R. Thangavel, A. G. Kannan, R. Ponraj, V. Thangavel, D.-W. Kim and Y.-S. Lee, *J. Power Sources*, 2018, **383**, 102–109.
37 C. Wang, Y. Fang, Y. Xu, L. Liang, M. Zhou, H. Zhao and Y. Lei, *Adv. Funct. Mater.*, 2016, **26**, 1777–1786.
38 H. Chen, M. Armand, G. Demailly, F. Dolhem, P. Poizot and J.-M. Tarascon, *ChemSusChem*, 2008, **1**, 348–355.
39 S. Rajendiran, K. Park, K. Lee and S. Yoon, *Inorg. Chem.*, 2017, **56**, 7270–7277.
40 S. Rajendiran, G. H. Gunasekar and S. Yoon, *New J. Chem.*, 2018, **42**, 12256–12262.
41 G. Zou, H. Hou, G. Zhao, Z. Huang, P. Ge and X. Ji, *Green Chem.*, 2017, **19**, 4622–4632.
42 J. Deng, M. Li and Y. Wang, *Green Chem.*, 2016, **18**, 4824–4854.
43 W. Luo, M. Allen, V. Raju and X. Ji, *Adv. Energy Mater.*, 2014, **4**, 1400554.
44 Y. Park, D.-S. Shin, S. H. Woo, N. S. Choi, K. H. Shin, S. M. Oh, K. T. Lee and S. Y. Hong, *Adv. Mater.*, 2012, **24**, 3562–3567.
45 R. Thangavel, A. Samuthira Pandian, H. V. Ramasamy and Y.-S. Lee, *ACS Appl. Mater. Interfaces*, 2017, **9**, 40187–40196.
46 D. Chao, P. Liang, Z. Chen, L. Bai, H. Shen, X. Liu, X. Xia, Y. Zhao, S. V. Savilov, J. Lin and Z. X. Shen, *ACS Nano*, 2016, **10**, 10211–10219.
47 M. Lee, J. Hong, J. Lopez, Y. Sun, D. Feng, K. Lim, W. C. Chueh, M. F. Toney, Y. Cui and Z. Bao, *Nat. Energy*, 2017, **2**, 861–868.
48 R. Thangavel, A. G. Kannan, R. Ponraj, X. Sun, D.-W. Kim and Y.-S. Lee, *J. Mater. Chem. A*, 2018, **6**, 9846–9853.
49 C. Xu, H. Wang, J. Deng and Y. Wang, *Sustainable Energy Fuels*, 2018, **2**, 357–360.
50 H. Kim, M.-Y. Cho, M.-H. Kim, K.-Y. Park, H. Gwon, Y. Lee, K. C. Roh and K. Kang, *Adv. Energy Mater.*, 2013, **3**, 1500–1506.
51 H. Du, H. Yang, C. Huang, J. He, H. Liu and Y. Li, *Nano Energy*, 2016, **22**, 615–622.
52 M. S. Kim, E. Lim, S. Kim, C. Jo, J. Chun and J. Lee, *Adv. Funct. Mater.*, 2017, **27**, 1603921.
53 E. Lim, C. Jo, M. S. Kim, M.-H. Kim, J. Chun, H. Kim, J. Park, K. C. Roh, K. Kang, S. Yoon and J. Lee, *Adv. Funct. Mater.*, 2016, **26**, 3553.

54 J. Yin, L. Qi and H. Wang, *ACS Appl. Mater. Interfaces*, 2012, **4**, 2762–2768.
55 D. P. Dubal, O. Ayyad, V. Ruiz and P. Gomez-Romero, *Chem. Soc. Rev.*, 2015, **44**, 1777–1790.
56 L. Zhou, Z. Yang, C. Li, B. Chen, Y. Wang, L. Fu, Y. Zhu, X. Liu and Y. Wu, *RSC Adv.*, 2016, **6**, 109340–109345.
57 J. Dong, Y. Jiang, Q. Li, Q. Wei, W. Yang, S. Tan, X. Xu, Q. An and L. Mai, *J. Mater. Chem. A*, 2017, **5**, 10827–10835.
58 H. Wang, C. Zhu, D. Chao, Q. Yan and H. J. Fan, *Adv. Mater.*, 2017, **29**, 1702093.
59 T. Wei, G. Yang and C. Wang, *ACS Appl. Mater. Interfaces*, 2017, **9**, 31861–31870.
60 L.-F. Que, F.-D. Yu, K.-W. He, Z.-B. Wang and D.-M. Gu, *Chem. Mater.*, 2017, **29**, 9133–9141.
61 M. Minakshi, D. Meyrick and D. Appadoo, *Energy Fuels*, 2013, **27**, 3516–3522.
62 I. Plitz, A. DuPasquier, F. Badway, J. Gural, N. Pereira, A. Gmitter and G. G. Amatucci, *Appl. Phys. A*, 2006, **82**, 615–626.
63 Z. Jian, V. Raju, Z. Li, Z. Xing, Y. S. Hu and X. Ji, *Adv. Funct. Mater.*, 2015, **25**, 5778–5785.
64 Z. Le, F. Liu, P. Nie, X. Li, X. Liu, Z. Bian, G. Chen, H. B. Wu and Y. Lu, *ACS Nano*, 2017, **11**, 2952–2960.
65 S. Liu, Z. Cai, J. Zhou, A. Pan and S. Liang, *J. Mater. Chem. A*, 2016, **4**, 18278–18283.
66 E. Lim, C. Jo, M. S. Kim, M.-H. Kim, J. Chun, H. Kim, J. Park, K. C. Roh, K. Kang, S. Yoon and J. Lee, *Adv. Funct. Mater.*, 2016, **26**, 3711–3719.
67 B. Li, F. Dai, Q. Xiao, L. Yang, J. Shen, C. Zhang and M. Cai, *Energy Environ. Sci.*, 2016, **9**, 102–106.
68 C. Liu, C. Zhang, H. Song, C. Zhang, Y. Liu, X. Nan and G. Cao, *Nano Energy*, 2016, **22**, 290–300.
69 F. Wang, C. Wang, Y. Zhao, Z. Liu, Z. Chang, L. Fu, Y. Zhu, Y. Wu and D. Zhao, *Small*, 2016, **12**, 6207–6213.
70 J. R. Rani, R. Thangavel, S.-I. Oh, J. M. Woo, N. Chandra Das, S.-Y. Kim, Y.-S. Lee and J.-H. Jang, *ACS Appl. Mater. Interfaces*, 2017, **9**, 22398–22407.